

A $0.24+0.18 M_{\odot}$ double-lined eclipsing binary from the HATSouth survey

G. Zhou,¹★ D. Bayliss,¹ J. D. Hartman,² M. Rabus,^{3,4} G. Á. Bakos,^{2,†} A. Jordán,³ R. Brahm,³ K. Penev,² Z. Csubry,² L. Mancini,⁴ N. Espinoza,³ M. de Val-Borro,² W. Bhatti,² S. Ciceri,⁴ T. Henning,⁴ B. Schmidt,¹ S. J. Murphy,⁵ R. P. Butler,⁶ P. Arriagada,⁶ S. Shectman,⁷ J. Crane,⁷ I. Thompson,⁷ V. Suc³ and R. W. Noyes⁸

¹Research School of Astronomy and Astrophysics, Australian National University, Canberra, ACT 2611, Australia

²Department of Astrophysical Sciences, Princeton University, NJ 08544, USA

³Instituto de Astrofísica, Pontificia Universidad Católica de Chile, Av. Vicuña Mackenna 4860, 7820436 Macul, Santiago, Chile

⁴Max Planck Institute for Astronomy, Königstuhl 17, D-69117 Heidelberg, Germany

⁵Astronomisches Rechen-Institut, Zentrum für Astronomie der Universität Heidelberg, D-69120 Heidelberg, Germany

⁶Department of Terrestrial Magnetism, Carnegie Institution of Washington, 5241 Broad Branch Road NW, Washington, DC 20015-1305, USA

⁷The Observatories of the Carnegie Institution of Washington, 813 Santa Barbara Street, Pasadena, CA 91101, USA

⁸Harvard-Smithsonian Center for Astrophysics, 60 Garden St, Cambridge, MA 02138, USA

Accepted 2015 May 8. Received 2015 May 8; in original form 2014 November 28

ABSTRACT

We report the discovery and characterization of a new M-dwarf binary, with component masses and radii of $M_1 = 0.244^{+0.003}_{-0.003} M_{\odot}$, $R_1 = 0.261^{+0.006}_{-0.009} R_{\odot}$, $M_2 = 0.179^{+0.002}_{-0.001} M_{\odot}$, $R_2 = 0.218^{+0.007}_{-0.011} R_{\odot}$, and orbital period of ~ 4.1 d. The M-dwarf binary HATS551–027 (LP 837–20) was identified as an eclipsing binary by the HATSouth survey, and characterized by a series of high-precision photometric observations of the eclipse events, and spectroscopic determinations of the atmospheric parameters and radial velocity orbits. HATS551–027 is one of few systems with both stellar components lying in the fully convective regime of very low mass stars, and can serve as a test for stellar interior models. The radius of HATS551–027A is consistent with models to 1σ , whilst HATS551–027B is inflated by 9 per cent at 2σ significance. We measure the effective temperatures for the two stellar components to be $T_{\text{eff},1} = 3190 \pm 100$ K and $T_{\text{eff},2} = 2990 \pm 110$ K; both are slightly cooler than theoretical models predict, but consistent with other M-dwarfs of similar masses that have previously been studied. We also measure significant $H\alpha$ emission from both components of the binary system, and discuss this in the context of the correlation between stellar activity and the discrepancies between the observed and model temperatures.

Key words: binaries: eclipsing – stars: individual: HATS551–027.

1 INTRODUCTION

Double-lined M-dwarf eclipsing binaries are natural laboratories for stellar astrophysics, providing the most precise, model independent, measurements for the fundamental stellar parameters of low-mass stars. They have been used extensively to test our theoretical understanding of stellar interiors (e.g. Chabrier & Baraffe 1995; Torres & Ribas 2002). Very low mass stars (VLMSs), with masses below $0.35 M_{\odot}$, are thought to have fully convective, adiabatic interiors (e.g. Chabrier & Baraffe 1997, 2000). Models have been unable

to match the observations of VLMSs, with measured temperatures cooler and radii larger than models predict (e.g. Torres & Ribas 2002; Ribas 2006; Torres, Andersen & Giménez 2010; Feiden & Chaboyer 2012; Spada et al. 2013; Torres 2013).

Double-lined M-dwarf binaries in the VLMS mass regime, where the stellar parameters have been accurately determined, are rare. The CM Draconis system is the most well studied, with masses and radii determined to better than 1 per cent precision (Lacy 1977; Metcalfe et al. 1996; Morales et al. 2009). The radius discrepancy between models and observations have been well documented for CM Draconis at the 2–10 per cent level (Torres & Ribas 2002; MacDonald & Mullan 2012; Spada et al. 2013; Feiden & Chaboyer 2014), depending on the treatment of metallicity, mixing length, and magnetic inhibition in the models. More recently, the systems KOI-126, Kepler-16, LSPM J1112+7626, and WTS 19g-4-02069

*E-mail: george.zhou@anu.edu.au

†Alfred P. Sloan Research Fellow.

‡Packard Fellow.

(Carter et al. 2011; Doyle et al. 2011; Irwin et al. 2011; Nefs et al. 2013) have been reported, with masses and radii of the low-mass stellar components measured to better than 2 per cent precision. Of these systems, only the radii of KOI-126B and C were found to be in agreement with the models of slightly supersolar metallicity, while the other VLMSs are inflated compared to the models (Feiden, Chaboyer & Dotter 2011; Spada & Demarque 2012; Nefs et al. 2013; Feiden & Chaboyer 2014).

A number of ideas have been put forward to explain the radius and temperature discrepancies between observations and the models. Increased metallicity and missing opacity may account for the larger measured radii of some systems (Berger et al. 2006; Burrows, Heng & Nampaisarn 2011). In particular, the KOI-126 B and C companions can be well modelled by assuming a metallicity of $[\text{Fe}/\text{H}] = +0.15$ (Feiden et al. 2011). However, López-Morales (2007) found that a metallicity–radius relationship exists for single stars, but not for binaries. Spada & Demarque (2012) suggested increased metallicity cannot fully account for the model discrepancy for the CM Draconis binary. Zhou et al. (2014) found no correlation between metallicity and the measured radii of the VLMS sample, suggesting that the effect of metallicity variation on radius is smaller than the present measurement uncertainties.

The spin-up of M-dwarfs in binary systems, leading to higher magnetic activities, has also been put forward to resolve the discrepancies (e.g. Chabrier, Gallardo & Baraffe 2007; López-Morales 2007). Chabrier et al. (2007) suggested that strong magnetic fields can inhibit convection and heat flow within the stars; increased spot coverage from higher magnetic activities will also modify the evolution of active low-mass stars, leading to different radii than inactive stellar models. This is supported by the empirical correlation between X-ray and H α activity levels and M-dwarf radii (López-Morales 2007; Morales, Ribas & Jordi 2008; Stassun et al. 2012). Models of the CM Draconis system by MacDonald & Mullan (2012, 2014) found that magnetic inhibition of convection can explain the radius discrepancy. However, Feiden & Chaboyer (2014) modelled the Kepler-16 and CM Draconis systems, and found it difficult to sustain the strong magnetic fields required to inhibit convection and inflate the stars to the observed radii.

Recently, accurate M-dwarf parameters have also become important for the characterization of the planets they host. The larger mass, radius, and luminosity ratios between M-dwarf hosts and planets make them enticing targets for discovery and follow-up characterization observations. The discrepancies in theoretical modelling of M-dwarfs resulted in a need for empirical relationships, derived from well-characterized M-dwarf measurements, in order to characterize the star and planet systems (e.g. Johnson et al. 2011, 2012; Hartman et al. 2015).

In this paper, we present the discovery and characterization of a new eclipsing, double-lined, M-dwarf binary, HATS551–027 (LP 837–20), with both stellar components firmly within the fully convective mass regime of VLMSs. HATS551–027 has previously been identified as a high proper motion (Luyten 1979; Salim & Gould 2003) M4.5 dwarf (Reid et al. 2003) from astrometric and low-resolution spectroscopic surveys of NLTT high proper motion stars. As part of our effort to characterize the VLMS population (Zhou et al. 2014), the HATSouth survey (Bakos et al. 2013) identified and characterized HATS551–027 as a low-mass eclipsing binary. We derive precise fundamental properties of the system via the discovery light curves and a series of photometric eclipse follow-up observations and spectroscopic orbit measurements, described in Sections 2 and 3. The HATS551–027 system is then discussed in the context of other VLMS binaries in Section 4.

2 OBSERVATIONS AND ANALYSIS

2.1 HATSouth photometric detection

The eclipses of HATS551–027 were first identified by observations from the HATSouth survey (Bakos et al. 2013). HATSouth is a global network of identical, fully robotic telescopes, providing continuous monitoring of selected 128 deg² fields of the southern sky. A total of 16 622 observations of HATS551–027 were obtained from HATSouth units HS-1, HS-2 in Chile, HS-3, HS-4 in Namibia, and HS-6 in Australia from 2009 September to 2010 September. Each HATSouth unit includes four 0.18 m f/2.8 Takahashi astrographs each with a Apogee 4 K \times 4 K U16M Alta CCD camera. The images have a field of view of 4° \times 4°, with a pixel scale of 3.7 arcsec pixel⁻¹. The observations are performed in the Sloan-*r'* band, at 4 min cadence. HATSouth photometry is detrended using the External Parameter Decorrelation (EPD; Bakos et al. 2007) and Trend Filtering Algorithm (TFA; Kovács, Bakos & Noyes 2005) techniques. The transit candidates search is performed with the Box-fitting Least Squares (Kovács, Zucker & Mazeh 2002) analysis. Details of the HATSouth reduction and analysis processes can be found in Bakos et al. (2013) and Penev et al. (2013). The HATSouth discovery light curve for HATS551–027 is displayed in Fig. 1, the photometric data can be found in Table 2.

2.2 Photometric follow-up

We performed photometric follow-up of the primary and secondary eclipses of HATS551–027. The observations are described below, summarized in Table 1, with the light curves plotted in Fig. 2 and found in Table 2. The specific set of reference stars and their magnitudes for differential photometry are listed in Table 3.

2.2.1 Faulkes Telescope South 2 m/Merope

Two secondary eclipses of HATS551–027 were observed by the Merope camera on 2-m Faulkes Telescope South (FTS), at Siding Spring Observatory, on 2012 December 12 and 2013 March 20. FTS/Merope has a field of view of 4.7 arcmin \times 4.7 arcmin, and a pixel scale of 0.139 arcsec pixel⁻¹, read out using 2 \times 2 binning mode. The observations were obtained in the *i* band, with exposure times of 60 s. The telescope was defocused to reduce the effect of intra- and interpixel variations on the final light curve, and to avoid saturation of target and reference stars. A total of 124 observations were obtained on 2012 December 12, and 114 on 2013 March 20.

Bias and flat-field reduced images, automatically generated by the LCOGT reduction pipeline, were used for the photometric extraction. The raw light curves for the target and reference stars were extracted using Source Extractor (Bertin & Arnouts 1996), via multiple fixed circular apertures, and after an interpolated background map was subtracted. Eleven reference stars of magnitudes $I = 12.1$ – 17.4 were used for the relative photometry. The best aperture was chosen to minimize the out-of-transit light-curve scatter. A second-order polynomial was fitted to the out-of-transit regions of the light curves to remove small, long-duration variations, likely due to changing air mass, before model fitting was performed.

2.2.2 Swope 1 m/SITE3

A near-complete primary eclipse of HATS551–027 was observed by the SITE#3 camera on the Swope 1 m telescope at Las Campanas Observatory, Chile, on 2013 February 26. Swope/SITE3 has a field

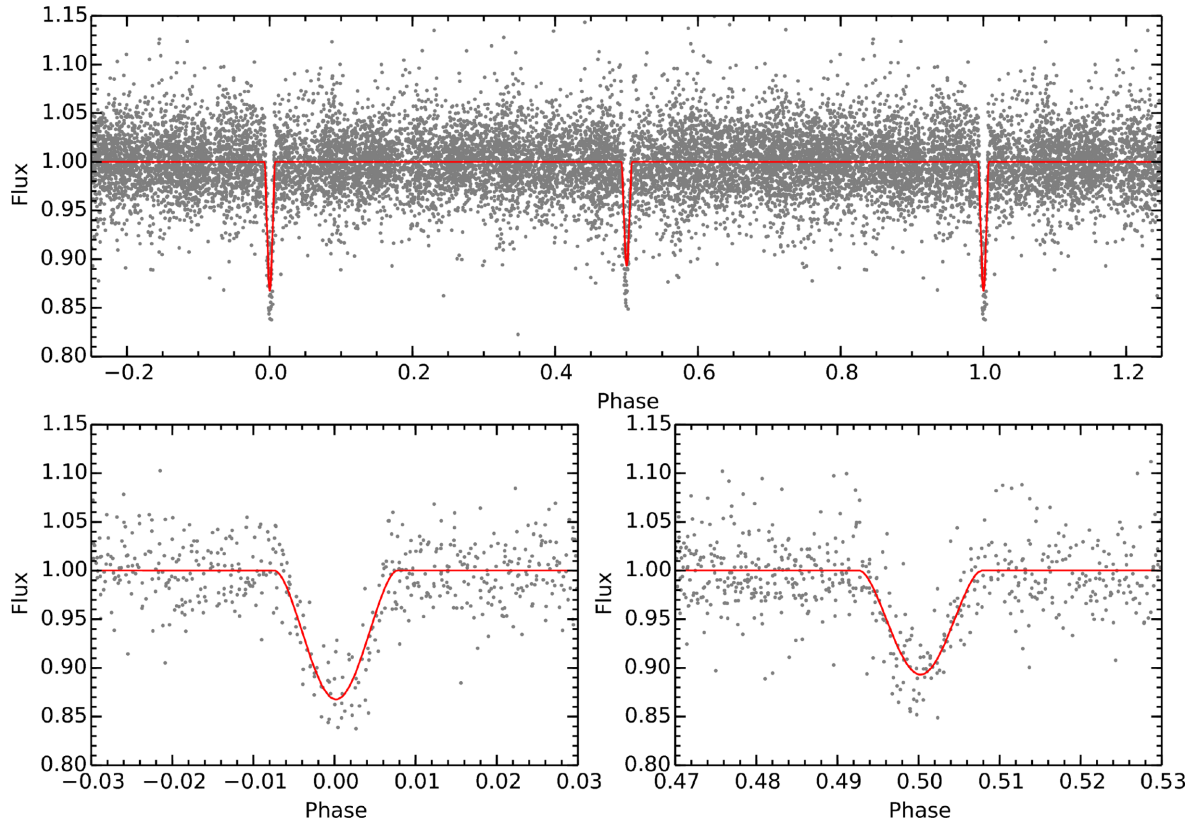


Figure 1. HATSouth discovery light curves of HATS551–027. The observations are plotted in grey, best-fitting model from Section 3.1 plotted in red. Close-ups of the primary and secondary eclipses are plotted in the lower panels.

Table 1. Summary of photometric observations.

Facility	Dates	Number of images	Exposure time (s)	Filter
HATSouth Network	2009 Sep–2010 Sep	16 622	240	i'
FTS/Merope	2012 Dec 12	124	60	i'
Swope/SITe3	2013 Feb 26	78	30	i'
FTS/Merope	2013 Mar 20	114	60	i'

of view of $14.8 \text{ arcmin} \times 22.8 \text{ arcmin}$, a pixel scale of $0.435 \text{ arcsec pixel}^{-1}$, and detector size of 2048×3150 pixels. The observations were performed in the i band, with 30 s exposures. A total of 78 exposures were obtained. Photometric extraction were performed on the reduced frames using the FITSH package (Pál 2012). Five reference stars of magnitudes $I = 12.7\text{--}13.5$ were used for the relative photometry. We note that no pre-ingress baseline was recorded, which may have an adverse effect on the derived timings and associated uncertainties.

2.3 Spectroscopic follow-up

We performed a series of spectroscopic follow-up observations at low, medium, and high resolution, to determine the stellar properties and orbit of the system. The observations are summarized in Table 4, and the radial velocities are plotted in Fig. 3 and presented in Table 5.

2.3.1 ANU 2.3 m/WiFeS

Spectroscopic observations at low and medium resolutions were performed using the Wide Field Spectrograph (WiFeS; Dopita

et al. 2007) on the ANU 2.3 m telescope, located at Siding Spring Observatory, Australia. WiFeS is an image slicer integral field spectrograph, with slitlets of 1 arcsec width in spatial coverage. The WiFeS observations provided the spectroscopic classification and radial velocities (to the $\sim 2 \text{ km s}^{-1}$ level) of HATS551–027.

For spectral classifications, an observation at low resolution of $\lambda/\Delta\lambda \equiv R = 3000$ was obtained using the B3000 and R3000 gratings on the blue and red arms of the spectrograph, with the RT560 dichroic, providing a flux-calibrated spectrum of the object over $3500\text{--}9000 \text{ \AA}$. For the $R = 3000$ observations, the stellar flux is summed over the three slitlets together to produce the final spectrum. Flux calibrations are performed according to Bessell (1999), using flux standard stars from Hamuy et al. (1992) and Bessell (1999) taken on the same night. The observational techniques, data reduction, and flux calibration processes for the WiFeS low-resolution observations are fully described in Bayliss et al. (2013).

To measure the radial velocity orbit, we then obtained 16 medium resolution ($R = 7000$) observations from 2012 September to 2014 August. The observations were performed using the R7000 grating and the RT480 dichroic, giving a velocity resolution of $21.6 \text{ km s}^{-1} \text{ pixel}^{-1}$ over the wavelength range $5200\text{--}7000 \text{ \AA}$,

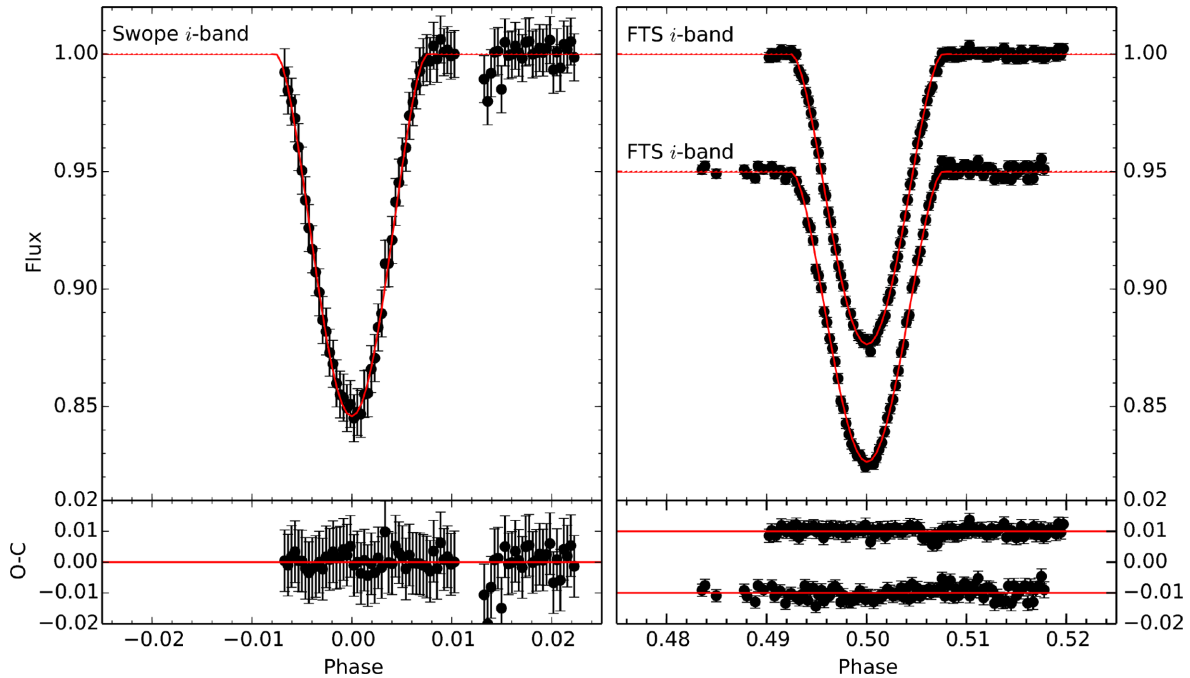


Figure 2. Follow-up photometric observations for the primary (left-hand panel) and secondary eclipses (right-hand panel) of HATS551–027. The observations are plotted in black, best-fitting model from Section 3.1 plotted in red. The uncertainties shown have been scaled up to force a reduced $\chi^2 = 1$ where necessary.

corresponding to the photometric R band. The wavelength calibrations were obtained from bracketing Fe–Ne–Ar arc lamp exposures. In addition, a first-order correction to the wavelength calibration is applied using the telluric Oxygen B lines over 6882–6906 Å. For radial velocity measurements, we reduce the spectra from each WiFeS slitlet separately, such that three reduced spectra from three slitlets are produced per exposure. The reduction process is described in detail in Bayliss et al. (2013). We adopted the $H\alpha$ -derived velocities for analysis in Section 3.1.

Radial velocities of both components of the binary were first measured by fitting the $H\alpha$ emission feature, which exhibits

clear and distinct signals from both stellar companions. For each spectrum, we fit the $H\alpha$ feature with two Gaussian components. The best-fitting values are obtained via a downhill simplex minimization using the PYTHON *fmin* function in SCIPY package, and the errors explored via a Markov chain Monte Carlo (MCMC) analysis using the EMCEE affine invariant ensemble sampler (Foreman-Mackey et al. 2013). The final velocity error from each exposure is a quadrature combination of the mean centroid errors from the MCMC fit and the scatter in velocity from three slitlets. The $H\alpha$ emission features and Gaussian fits for each observation are presented in Fig. 4. The observations from each night are plotted by three black solid lines,

Table 2. HATS551–027 differential photometry.

BJD	Flux	Δ Flux	Instrument	Filter
2455083.75892	0.9999	0.0236	HATSouth ^a	r'
2455083.76216	1.0084	0.0192	HATSouth	r'
2455083.76552	1.0514	0.018	HATSouth	r'
2455083.76873	0.9989	0.0209	HATSouth	r'
2455083.7721	0.9632	0.0221	HATSouth	r'
2455083.77532	0.9487	0.0204	HATSouth	r'
2455083.77868	1.0744	0.0173	HATSouth	r'
2455083.78191	0.9683	0.02	HATSouth	r'
2455083.78528	1.0118	0.0196	HATSouth	r'
2455083.78849	1.014	0.0188	HATSouth	r'

Note. This table is available in a machine-readable form in the online journal. A portion is shown here for guidance regarding its form and content.

^aFor the HATSouth light curve these magnitudes have been detrended using the EPD and TFA procedures prior to fitting a transit model to the light curve. Primarily as a result of this detrending, but also due to blending from neighbours, the apparent HATSouth transit depth is ~ 90 per cent that of the true depth in the Sloan r filter.

Table 3. Summary of reference stars for follow-up photometry.

Reference star	RA	Dec.	I mag
FTS 2012-12-12/2013-03-20			
1	+05:44:56.682	–24:57:43.844	12.1
2	+05:44:48.663	–24:56:55.899	14.9
3	+05:45:03.111	–24:56:18.213	15.0
4	+05:44:59.082	–24:54:44.068	15.7
5	+05:45:02.925	–24:54:28.156	15.8
6	+05:44:56.505	–24:54:12.312	16.3
7	+05:44:49.306	–24:56:45.252	16.2
8	+05:45:06.857	–24:55:22.837	16.6
9	+05:45:03.468	–24:56:38.683	17.4
10	+05:44:51.649	–24:54:24.864	17.0
11	+05:45:02.931	–24:55:32.118	15.3
Swope 2013-02-26			
1	+05:45:29.156	–24:49:56.572	12.7
2	+05:45:23.524	–24:51:07.124	13.0
3	+05:44:32.656	–24:54:16.506	13.4
4	+05:44:30.314	–24:54:57.665	13.5
5	+05:45:10.934	–25:02:41.212	13.2

Table 4. Summary of spectroscopic observations.

Facility	Date range	Number of observations	Resolution	S/N ^a
ANU 2.3 m/WiFeS	2012 Sep 8	1	3000	95
ANU 2.3 m/WiFeS	2012 Sep 8–2014 Aug 14	16	7000 (<i>R</i> band)	20
MPG/ESO 2.2 m/FEROS	2013 Mar 24–27	4	48 000	35
Magellan 6.5 m/PFS	2013 Feb 21	4	76 000	90
ANU 2.3 m/WiFeS	2014 Sep 6–2014 Oct 10	3	7000 (<i>I</i> Band)	60

Note. ^aAverage signal-to-noise ratio per resolution element, at approximate peak.

for the spectra from the three slitlets. The best-fitting Gaussians for each spectrum are also plotted by the dotted line, in red for the primary component, blue for the secondary component. The velocities from WiFeS are presented in Fig. 3 and Table 5.

We also tried cross-correlations between the target spectra and an M4V template from a WiFeS observation of the standard star LP 816–60. The radial velocity standard cross-correlations provided blended cross-correlation functions (CCFs), which did not resolve the two spectral components as well as the H α feature. We derived radial velocities from selected WiFeS R7000 observations taken at phase quadrature by simultaneously fitting a double Gaussian to the CCF profile, presented in Fig. 3 and Table 5. We also tried cross-correlating against spectral templates from the BT-Settl model atmospheres (Allard et al. 2012), but we could not resolve the two spectral components.

The WiFeS cross-correlations were also used to measure light ratio between the two stellar components (L_2/L_1). We fit a double Gaussian to the CCFs from the spectra, and derived a light ratio of 0.53 ± 0.06 from the R7000 grating, equivalent of the photometric *R* band. We also obtained three additional exposure over the wavelength range 6800–9100 Å at $R = 7000$, using I7000 grating and the RT615 dichroic, corresponding to the photometric *I* band. This exposure was used to measure the light ratio between the two components at the wavelength of the follow-up photometric observations. The I7000 observation gave a light ratio of 0.50 ± 0.01 , consistent to the *R*-band light ratio.

2.3.2 MPG 2.2 m/FEROS

Four observations of HATS551–027 were obtained using the fibre-fed FEROS spectrograph on the MPG 2.2 m telescope at La Silla Observatory, Chile, over the nights 2013-03-24 to 2013-03-27. FEROS provides a resolution of $R = 48\,000$; descriptions of the FEROS observations and reduction procedures can be found in Penev et al. (2013), Jordán et al. (2014), and Brahm et al. (2015). The observations are cross-correlated with an M-dwarf template. The two components of the binary are fully separated in the CCF, and the velocities are presented in Fig. 3 and Table 5. We also measure the Gaussian peak heights of the CCFs to estimate the light ratio for the two components of the system. Because of the faintness of the target star, we find that two orders in the wavelength range 6475–6665 Å reliably showed the two CCF peaks in all of the exposures. The average and standard deviation CCF peak heights over the four exposures was 0.42 ± 0.07 .

2.3.3 Magellan 6.5 m/PFS

Four consecutive observations of HATS551–027 were obtained using the Carnegie Planet Finder Spectrograph (PFS; Crane et al. 2010) on Magellan II, Las Campanas Observatory, Chile, on the night of 2013-02-21 UT. The observations were taken through the iodine cell, with a 0.5 arcsec \times 2.5 arcsec slit and using 2×2 binning in slow read-out mode.

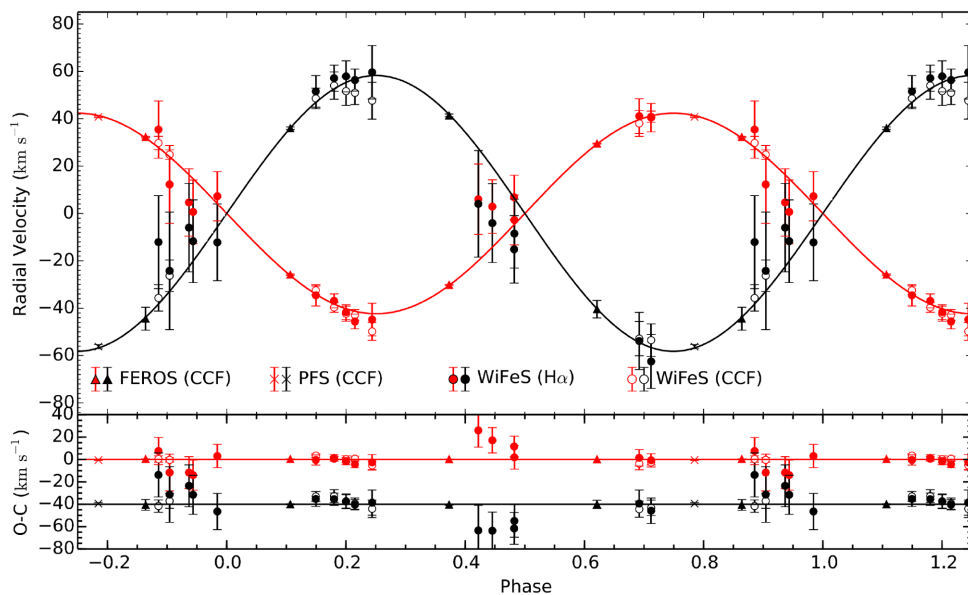


Figure 3. The radial velocity orbit of HATS551–027A (red) and B (black). The best-fitting models from Section 3.1 are plotted by the red and black curves for components A and B, respectively.

Table 5. HATS551–027 radial velocities.

HJD	RV ₁ (km s ⁻¹) ^a	σRV ₁ (km s ⁻¹)	RV ₂ (km s ⁻¹)	σRV ₂ (km s ⁻¹)	Instrument
2456179.31471	-0.8	6.9	103.7	11.3	WiFeS (Hα)
2456179.31471	-25.8	3.3	70.9	6.7	WiFeS (CCF)
2456180.28765	41.3	10.5	35.5	14.6	WiFeS (Hα)
2456198.23861	79.5	12.1	32.0	19.7	WiFeS (Hα)
2456198.23861	55.1	2.5	-9.9	4.7	WiFeS (CCF)
2456231.09138	44.7	13.5	32.3	17.4	WiFeS (Hα)
2456375.98307	50.9	9.3	28.9	14.2	WiFeS (Hα)
2456378.02998	51.3	10.4	31.8	16.2	WiFeS (Hα)
2456378.97110	-1.6	3.1	100.4	4.6	WiFeS (Hα)
2456378.97110	-18.9	2.1	74.3	4.3	WiFeS (CCF)
2456380.99658	84.5	6.0	-18.4	11.4	WiFeS (Hα)
2456380.99658	66.2	2.1	-26.8	6.2	WiFeS (CCF)
2456876.30644	2.4	3.1	102.0	6.6	WiFeS (Hα)
2456876.30644	-18.3	2.8	75.3	5.1	WiFeS (CCF)
2456877.30697	46.9	11.3	40.0	16.7	WiFeS (Hα)
2456878.31132	85.1	7.3	-9.8	12.1	WiFeS (Hα)
2456878.31132	63.3	4.8	-26.8	6.2	WiFeS (CCF)
2456879.30918	48.7	14.2	38.1	18.7	WiFeS (Hα)
2456880.30174	7.1	2.9	101.2	5.5	WiFeS (Hα)
2456880.30174	-15.8	1.7	76.6	4.7	WiFeS (CCF)
2456881.28823	50.1	14.9	48.1	22.5	WiFeS (Hα)
2456883.25386	56.3	16.4	19.8	24.8	WiFeS (Hα)
2456883.25386	50.0	1.6	-0.5	5.6	WiFeS (CCF)
2456884.25377	9.5	4.5	95.6	6.7	WiFeS (Hα)
2456884.25377	-8.5	1.6	71.5	3.8	WiFeS (CCF)
2456375.53799	-5.8	0.2	65.7	0.6	FEROS
2456376.54952	53.8	0.2	-16.1	3.7	FEROS
2456377.53960	56.6	0.3	-20.1	4.8	FEROS
2456378.52904	-1.5	0.3	60.4	0.5	FEROS
2456344.60054	3.2	0.3	-93.8	0.9	PFS

Note. ^aThe zero-point of these velocities is arbitrary. An offset is added to each instrument independently in the global fitting.

We use the PFS spectrum to derive the single epoch relative radial velocities and light ratio of the two stellar components. The spectra from the four observations were averaged, and cross-correlated against a $T_{\text{eff}} = 3100\text{ K}$, $\log g = 5.0$ solar metallicity BT-Settl synthetic spectrum (Allard et al. 2012). We used five orders outside of the Iodine absorption region (6114–6574 Å) for the cross-correlation. The two stellar components are resolved and fully separated in the CCF. We simultaneously fit two Gaussians to the CCF, deriving the light ratios and the velocity centroids. The velocities from the five orders are weight averaged to arrive at the final relative velocity between the two stellar components. The light ratio L_2/L_1 is 0.51 ± 0.04 , with the error as the standard deviation between the five orders. We also tried 3000 and 3200-K synthetic templates, yielding the same light ratio to within ± 0.01 . The light ratio measured from PFS is also consistent to $\sim 1\sigma$ of that measured from the FEROS spectra and WiFeS spectra. We adopt the light ratio measured from the high signal-to-noise (S/N) PFS observations for our modelling in Section 3.1.

3 SYSTEM PARAMETERS

3.1 Global modelling of light curves and radial velocities

We perform a global modelling of the HATSouth discovery light curves, follow-up photometry, and spectroscopic radial velocities to derive the system parameters for HATS551–027. We model the light curves according to Nelson & Davis (1972), using a modified

version of the JKTEBOP code (Popper & Etzel 1981; Southworth, Maxted & Smalley 2004). The radial velocities are modelled using Keplerian orbits.

The free parameters of the fit are period P , reference transit time t_0 , radius ratio R_2/R_1 , normalized radius sum $(R_1 + R_2)/a$, line-of-sight inclination i , light ratio L_2/L_1 , orbital eccentricity parameters $e \cos \omega$ and $e \sin \omega$, and orbital semi-amplitudes K_1 , K_2 for the two components. We assign a Gaussian prior to L_2/L_1 (following, e.g. Irwin et al. 2011) from the PFS light ratio of 0.51 ± 0.04 from Section 2.3.3. Without the prior, the radius ratio becomes degenerate with the light ratio, and is difficult to constrain. We assume uniform priors for all other free parameters. The quadratic limb darkening coefficients for both components are fixed to that from Claret (2000) using the PHOENIX models, and given in Table 6. At each iteration, the modelled mass ratio ($q = K_1/K_2$) is used to calculate the ellipsoidal variability expected in the light curve. Following Morales et al. (2009), we assign fixed reflection albedos for both components of 0.5, and gravity darkening coefficients of 0.2. The instrument zero-points for each data set are not included as free parameters in the global model, but rather fitted for at each iteration independently. We often find the HATSouth discovery light curves to be diluted due to the TFA detrending that was applied, as well as third-light blending from nearby neighbours due to the larger pixel scales of the instrument. The model transit shape is significantly constrained by the follow-up observations, and can be used to correct for the dilution of the HATSouth light curves. At each iteration, we adjust the transit depth of the HATSouth light curves

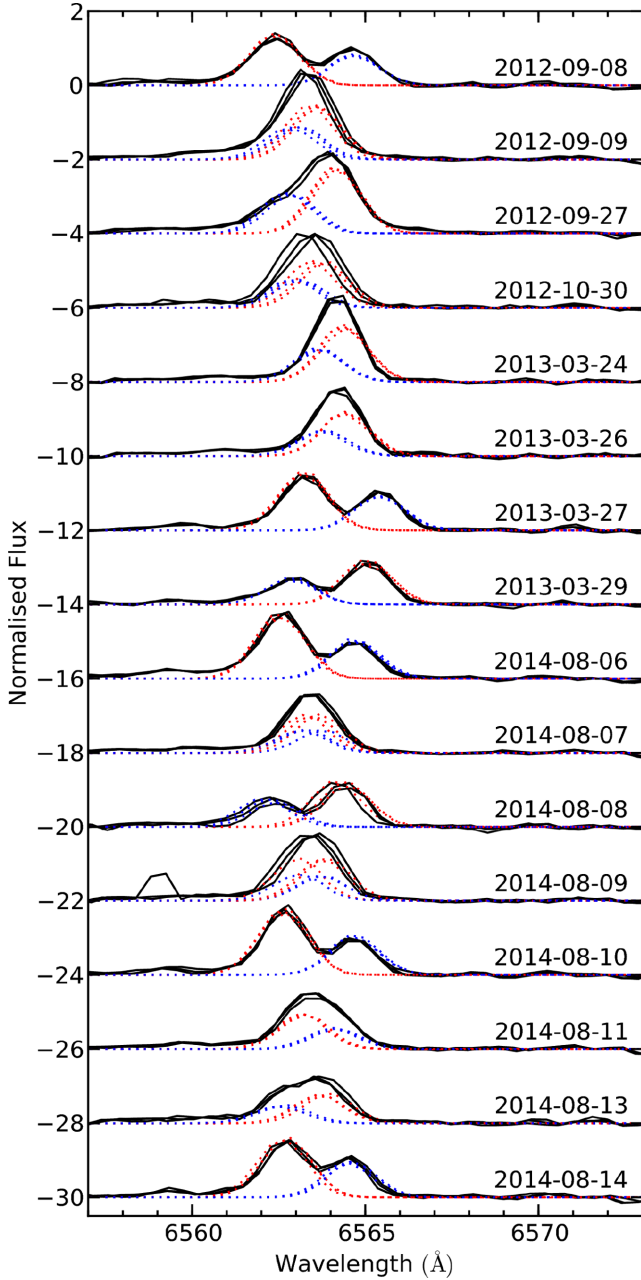


Figure 4. The $H\alpha$ emission feature from the WiFeS $R = 7000$ observations. For each exposure, the spectra from the three slitlets are plotted individually, in black. The best-fitting profiles are plotted in red for the primary component, and blue for the secondary component. Each exposure is arbitrarily offset in flux by 2 for clarity.

to the tested model by fitting for a third-light component (e.g. Zhou et al. 2014). We adopt the WiFeS radial velocities derived from the $H\alpha$ emission line in our analysis, since the two stellar components are better resolved in $H\alpha$ than in the CCFs.

The best-fitting parameters and the associated uncertainties are explored via an MCMC analysis, using `EMCEE`. For each MCMC run, we initialize 100 walkers over 2500 steps each. The walkers are initialized with randomized starting positions around their respective expected best-fitting parameter values. Examination of the MCMC chain shows that convergence is generally reached after 500–1000 steps, depending on the initial conditions. We then

Table 6. HAT551–027 system modelling parameters.

Parameter	Value	Source
Modelled system parameters		
Period (d)	$4.077017 \begin{pmatrix} +1 \\ -1 \end{pmatrix}^a$	GM ^b
T_0 (BJD)	$2456374.0171 \begin{pmatrix} +1 \\ -2 \end{pmatrix}$	GM
$(R_1 + R_2)/a$	$0.0590 \begin{pmatrix} +5 \\ -3 \end{pmatrix}$	GM
R_2/R_1	$0.82 \begin{pmatrix} +5 \\ -3 \end{pmatrix}$	GM
i ($^\circ$)	$87.99 \begin{pmatrix} +3 \\ -3 \end{pmatrix}$	GM
L_2/L_1 (6114–6574 Å)	$0.56 \begin{pmatrix} +6 \\ -8 \end{pmatrix}$	GM+PFS
L_2/L_1 (R-band)	$0.53 \begin{pmatrix} +6 \\ -6 \end{pmatrix}$	WiFeS
L_2/L_1 (I-band)	$0.50 \begin{pmatrix} +1 \\ -1 \end{pmatrix}$	WiFeS
$e \cos \omega$	$0.00013 \begin{pmatrix} +7 \\ -6 \end{pmatrix}$	GM
$e \sin \omega$	$-0.002 \begin{pmatrix} +1 \\ -2 \end{pmatrix}$	GM
K_1 (km s ⁻¹)	$42.4 \begin{pmatrix} +2 \\ -1 \end{pmatrix}$	GM
K_2 (km s ⁻¹)	$57.6 \begin{pmatrix} +4 \\ -3 \end{pmatrix}$	GM
R-band star A u_1	0.3762	Fixed ^c
R-band star A u_2	0.4574	Fixed ^c
R-band star B u_1	0.5392	Fixed ^c
R-band star B u_2	0.3485	Fixed ^c
i-band star A u_1	0.1539	Fixed ^c
i-band star A u_2	0.6330	Fixed ^c
i-band star B u_1	0.3124	Fixed ^c
i-band star B u_2	0.5509	Fixed ^c
Gaussian process modelling parameters		
A (FTS 20121212)	$0.0005 \begin{pmatrix} +2 \\ -2 \end{pmatrix}$	GM
τ (FTS 20121212) (d)	$0.0013 \begin{pmatrix} +1 \\ -1 \end{pmatrix}$	GM
A (Swope 20130226)	$0.0022 \begin{pmatrix} +6 \\ -5 \end{pmatrix}$	GM
τ (Swope 20130226) (d)	$0.0037 \begin{pmatrix} +4 \\ -2 \end{pmatrix}$	GM
A (FTS 20130320)	$0.0004 \begin{pmatrix} +3 \\ -4 \end{pmatrix}$	GM
τ (FTS 20130320) (d)	$0.0019 \begin{pmatrix} +1 \\ -2 \end{pmatrix}$	GM
Derived parameters		
M_1 (M_\odot)	$0.244 \begin{pmatrix} +3 \\ -3 \end{pmatrix}$	GM
R_1 (R_\odot)	$0.261 \begin{pmatrix} +6 \\ -9 \end{pmatrix}$	GM
M_2 (M_\odot)	$0.179 \begin{pmatrix} +2 \\ -1 \end{pmatrix}$	GM
R_2 (R_\odot)	$0.218 \begin{pmatrix} +7 \\ -11 \end{pmatrix}$	GM

Notes. ^aUncertainties in parenthesis for the last significant figure.

^bGM – global modelling of light curves and radial velocities.

^cFixed to values interpolated from Claret (2000) using the PHOENIX models.

re-run the MCMC with walkers initialized around the best-fitting parameters from the first run. We inflate the per-point measurement uncertainties such that the reduced χ^2 for each data set is at unity with respect to the best-fitting parameters derived from the first MCMC run. This allows other sources of error unaccounted for in data reduction to be included in the MCMC analysis. We found that only the FTS observations required their measurement uncertainties to be inflated by 2.4 times and 2.1 times for the 2012-12-12 and 2013-03-20 observations, respectively.

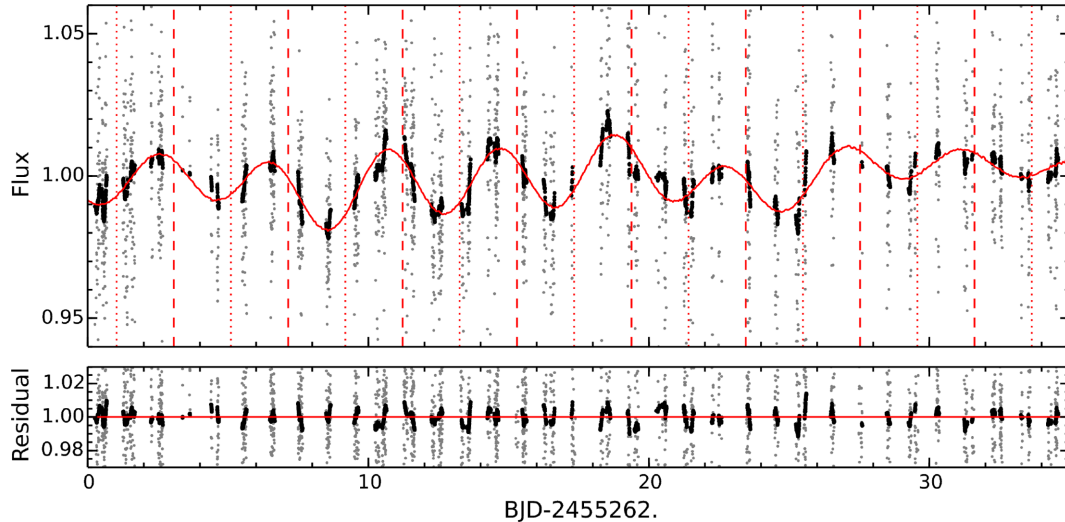


Figure 5. A 35-d sample segment of the HATSouth light curve residuals to the best-fitting model from Section 3.1. The data points are plotted in grey, 50 point-width boxcar smoothed function in black, and the cosine filtering model by the red line. The times of transits and eclipses, masked out in the data, are marked by vertical red dashed and dotted lines, respectively. The corrected data are plotted on the bottom panel.

3.1.1 Accounting for spots

Late M-dwarfs are known to be active, and the presence of chromospheric spectral emission features of HATS551–027 suggest that it is no exception. A Lomb–Scargle (Lomb 1976; Scargle 1982) analysis of the out-of-transit HATSouth light curve residuals from Section 3.1 shows a highest peak at 4.24 d, with peak full width at half-maximum of 0.08 d, compared to an orbital period of 4.08 d. Although when we break the light curve into four segments of 4000 points each, we cannot demonstrate the consistency of the peak location.

Star-spot activities affect the observations and model results in several ways. First, they induce periodically modulated out-of-transit variations in the HATSouth light curves. We correct this by modelling the cosine filtered light curve in the MCMC analysis. We model the modulation in the HATSouth light curve residuals using a set of linearly combined cosine functions, following equation (1) of Huang, Bakos & Hartman (2013). The HATSouth light-curve residuals, with transits and eclipses masked, are smoothed by a 50 point-width boxcar, and fitted with the cosine filtering model with minimum period of $P/2$ and maximum period of twice the observational baseline. The light-curve residuals and cosine filtering model for a segment of the HATSouth observations are shown in Fig. 5. The cosine filtering model has a standard deviation of 0.006, and peak-to-peak amplitudes of ~ 2 per cent. For comparison, the modelled out-of-transit variations originating from reflection and ellipsoidal effects is at the 10^{-4} level.

Variations in spot coverage also alters the total flux of the system, leading to variations in the eclipse depth. This affects the parameters derived from the high-precision follow-up photometry, such as R_2/R_1 and $(R_2 + R_1)/a$. Since the follow-up observations were performed ~ 800 d after the end of the HATSouth continuous observations, they cannot be corrected by employing spot model fits to the out-of-transit variability (e.g. Morales et al. 2009). Instead, we create 100 different sets of the follow-up light curves, with each light curve scaled by a random factor drawn from a Gaussian distribution with $\mu = 1.0$ and $\sigma = 0.006$ (the standard deviation of the cosine filtering model). We then perform a global analysis detailed in Section 3.1 using the scaled sets of the follow-up light

curves. The MCMC chains from each of the 100 separate analyses are combined to provide the final system uncertainties.

In-transit star-spot crossing events modify the shape of the transit light curve, and can be identified from the correlated red-noise in the fit residuals. Whilst we cannot correct for the spot crossing events, we can account for their effects in the uncertainties of the model fit. To account for correlated noise, we treat the follow-up photometry as a Gaussian process (e.g. Gibson et al. 2012). We form the covariance matrix Σ , of dimension $N \times N$, where N is the number of data points per follow-up light curve. The elements of the covariance matrix are defined as

$$\Sigma_{ij} = A^2 \exp\left(-\frac{(t_i - t_j)^2}{2\tau^2}\right) + \sigma_i^2 \delta_{ij}, \quad (1)$$

where A and τ are free parameters in the MCMC describing the amplitude and time-scale of the covariance function, and σ_i is the uncorrelated uncertainty for measurement i . The log likelihood \mathcal{L} for the residuals \mathbf{r} is calculated as

$$\log \mathcal{L} = -\frac{1}{2} \mathbf{r}^T \Sigma^{-1} \mathbf{r} - \frac{1}{2} \log |\Sigma| - \frac{N}{2} \log(2\pi). \quad (2)$$

The Gaussian process modelling provides more realistic uncertainty estimates. The A and τ factors are presented in Table 6.

3.1.2 Results

The final masses and radii are $M_1 = 0.244^{+0.003}_{-0.003} M_\odot$, $R_1 = 0.261^{+0.006}_{-0.009} R_\odot$, $M_2 = 0.179^{+0.002}_{-0.001} M_\odot$, $R_2 = 0.216^{+0.007}_{-0.011} R_\odot$. The full set of system parameters are presented in Table 6. The results presented are the mode of the posterior probability distributions, with the uncertainties representing the 68 per cent confidence region.

The posterior probability distributions for the free parameters in our global fit are shown in Fig. 6. For each pair of parameters, we calculate the Pearson R correlation coefficient to check for degeneracies. We note a significant degeneracy between the light ratio L_2/L_1 and the radius ratio R_2/R_1 in our results. For systems with partial eclipses, it is difficult to constrain both parameters simultaneously purely from the transit light curves without a prior on the

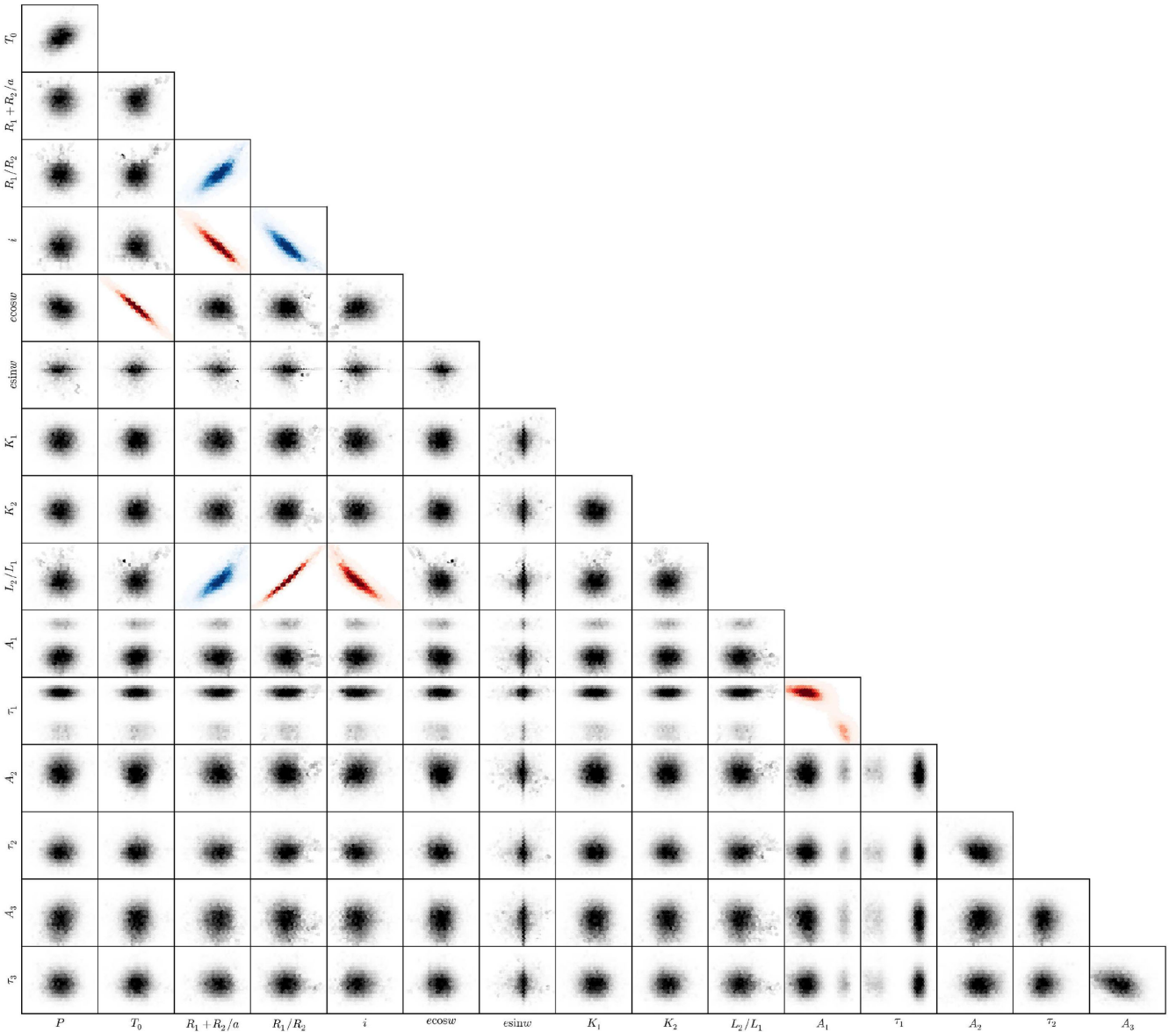


Figure 6. Posterior correlation diagrams for the free parameters in the global fit. Pairs of parameters with Pearson correlation coefficient of $0.5 < R < 0.8$ are coloured in blue, $R > 0.8$ coloured in red.

light ratio. We also note a correlation between $(R_1 + R_2)/a$ and inclination i , since both parameters together determine the transit shape. The time parameters T_0 and $e \cos \omega$ are correlated, since the phase of the secondary eclipse, determined by $e \cos \omega$, is influenced by the ephemeris of the primary transit T_0 . We examined the posterior probability distributions for the mass and radius of both stars, and found no correlation between the derived mass versus radius distribution.

3.1.3 Testing the robustness of the results

To test the dependence of our results against various assumptions and data sets, we re-ran the full MCMC analysis with different subsets of data and initial parameters. For each test, we describe the changes to the free parameters, assumptions, and data sets used, and report the major differences of the derived results to those

reported in Table 6. While these tests provide a useful guide for gauging the robustness of our results, the uncertainty estimates we report are likely still optimistic, as they are largely dependent on the per-point measurement uncertainties. Only repeated velocity measurements and photometric follow-up observations will provide the most robust stellar properties for HATS551–027.

(i) We set limb darkening coefficients as free parameters, but found that we can only place very weak constraints on the coefficients from the fitting. In R band, component A has best-fitting limb darkening coefficients of $u_1 = 0.5^{+0.5}_{-0.3}$, $u_2 = 0.3^{+0.4}_{-0.4}$, component B of $u_1 = 0.7^{+0.5}_{-0.3}$, $u_2 = 0.0^{+0.3}_{-0.4}$, and in I band, component A of $u_1 = 0.7^{+0.9}_{-0.5}$, $u_2 = 0.1^{+0.7}_{-0.5}$, component B of $u_1 = 0.7^{+0.9}_{-0.5}$, $u_2 = 0.1^{+0.6}_{-0.6}$. We found the limb darkening parameters were largely orthogonal to the other parameters. The resulting best-fitting parameter values did not differ significantly between the limb darkening

free and fixed analyses, and the radii and mass uncertainties were not noticeably inflated by freeing the limb darkening parameters.

(ii) To test the effect of the single epoch of PFS velocities on the resulting derived masses, we refit the observations without the PFS velocities. The resulting orbit semi-amplitudes were $K_1 = 42.4^{+0.1}_{-0.2} \text{ km s}^{-1}$ and $K_2 = 58.0^{+0.6}_{-0.4} \text{ km s}^{-1}$, yielding masses of $M_1 = 0.249^{+0.004}_{-0.005} M_\odot$ and $M_2 = 0.181^{+0.002}_{-0.002} M_\odot$. The derived properties are consistent with the global fit results to within errors.

(iii) To test if the $H\alpha$ -derived velocities, which reflect velocities of the chromosphere, are representative of the photospheric velocities, we fit the system using only WiFeS CCF-derived velocities. We derived velocity semi-amplitudes of $K_1 = 44.1^{+0.9}_{-1.0} \text{ km s}^{-1}$ and $K_2 = 53.2^{+2.2}_{-2.2} \text{ km s}^{-1}$, yielding masses of $M_1 = 0.21^{+0.02}_{-0.02} M_\odot$ and $M_2 = 0.18^{+0.01}_{-0.01} M_\odot$. In comparison, using only the WiFeS $H\alpha$ -derived velocities, we derive semi-amplitudes of $K_1 = 43.3^{+1.4}_{-1.4} \text{ km s}^{-1}$ and $K_2 = 59.7^{+2.0}_{-2.6} \text{ km s}^{-1}$, yielding masses of $M_1 = 0.26^{+0.02}_{-0.02} M_\odot$ and $M_2 = 0.19^{+0.01}_{-0.01} M_\odot$. The discrepancy between the K_2 values is likely due to the difficulties in resolving and fitting the secondary CCF and $H\alpha$ component using the lower resolution spectra. The derived semi-amplitudes and masses are consistent to the global fit results to within 2σ .

(iv) To test the dependence of the results on the four FEROS measurements and associated uncertainties, we fit the data set with only the FEROS velocities and derive velocity semi-amplitudes of $K_1 = 42.4^{+0.2}_{-0.3} \text{ km s}^{-1}$ and $K_2 = 57.8^{+1.3}_{-0.5} \text{ km s}^{-1}$, yielding masses of $M_1 = 0.247^{+0.010}_{-0.009} M_\odot$ and $M_2 = 0.182^{+0.004}_{-0.005} M_\odot$. The masses determined are consistent, but have three times larger uncertainties from the global fit. To check the dependence of our derived masses against the measurement precision, we inflate the FEROS uncertainties by two times, and refit using only the inflated FEROS velocities, deriving semi-amplitudes of $K_1 = 42.4^{+0.5}_{-0.5} \text{ km s}^{-1}$ and $K_2 = 58.0^{+1.8}_{-2.0} \text{ km s}^{-1}$, yielding masses of $M_1 = 0.248^{+0.017}_{-0.018} M_\odot$ and $M_2 = 0.181^{+0.007}_{-0.009} M_\odot$. Inflating the velocity measurement uncertainty by two times leads to a ~ 2 times inflation of the derived mass uncertainties.

(v) In Section 3.1.1, we tried to account for spot-induced uncertainties by (1) Monte Carlo of out-of-transit baseline flux and (2) addition of Gaussian processes modelling. To test their effects, we removed the two treatments and refit the data. The derived radius ratio is $R_2/R_1 = 0.82^{+0.03}_{-0.04}$, light ratio $L_2/L_1 = 0.53^{+0.04}_{-0.05}$, resulting stellar radii of $R_1 = 0.260^{+0.006}_{-0.004} R_\odot$, and $R_2 = 0.214^{+0.006}_{-0.006} R_\odot$. Note the significant reduction in the estimated uncertainties (~ 60 per cent) without accounting for spot activity.

(vi) To test the dependence of the results on the systematic errors associated with each FTS secondary eclipse observation, and the polynomial normalization applied to the light curves, we fit the observations using each FTS secondary eclipse observation independently. Using the FTS 2012-12-12 light curves for the secondary eclipse, we derive a radius ratio of $R_2/R_1 = 0.84^{+0.06}_{-0.07}$, light ratio $L_2/L_1 = 0.55^{+0.09}_{-0.09}$, resulting stellar radii of $R_1 = 0.259^{+0.009}_{-0.007} R_\odot$ and $R_2 = 0.22^{+0.01}_{-0.01} R_\odot$. Using the FTS 2013-03-20 light curves for the secondary eclipse, we derive a radius ratio of $R_2/R_1 = 0.81^{+0.07}_{-0.07}$, light ratio $L_2/L_1 = 0.52^{+0.09}_{-0.10}$, resulting stellar radii of $R_1 = 0.262^{+0.010}_{-0.008} R_\odot$, and $R_2 = 0.22^{+0.01}_{-0.02} R_\odot$. In each case, the derived values are consistent, with the uncertainties for the radius and light ratio parameters increased by ~ 30 per cent.

(vii) In the Swope light curve, four measurements at phase ~ 0.15 were consistently below the out-of-transit median. We masked out the outlying measurements and performed the refit, deriving a radius ratio of $R_2/R_1 = 0.84^{+0.05}_{-0.05}$, light ratio $L_2/L_1 = 0.55^{+0.07}_{-0.07}$, resulting

stellar radii of $R_1 = 0.261^{+0.006}_{-0.007} R_\odot$ and $R_2 = 0.22^{+0.01}_{-0.01} R_\odot$. The differences are negligible compared to the global fit.

(viii) We note that the follow-up photometric observations were all obtained in the i band. Single-band follow-up observations can bias the derived radius ratio parameters if the light ratio is band-dependent. For comparison, we fit the observations using the r -band HATSouth observations only, without the photometric follow-up data sets, we derive $T_0 = 2456374.017^{+0.002}_{-0.002}$ (consistent, but ten times worse in precision), $(R_1 + R_2)/a = 0.060^{+0.002}_{-0.002}$ (consistent but four times worse in precision), $R_2/R_1 = 0.83^{+0.04}_{-0.05}$ (consistent and equal precision), light ratio of $L_2/L_1 = 0.52^{+0.04}_{-0.07}$ (consistent and equal precision), and component radii of $R_1 = 0.267^{+0.009}_{-0.012}$ and $R_2 = 0.22^{+0.01}_{-0.01}$ (a larger R_1 , but still consistent within 1σ).

(ix) The light ratio L_2/L_1 in our global fit is tightly constrained by a Gaussian prior of mean 0.51 and standard deviation 0.04, determined by the analyses of the PFS spectra. To understand the effect of this prior on our resulting parameters, we modify to the Gaussian prior to have a mean 0.51 and standard deviation 0.08 (two times broader). The resulting fit has a $R_2/R_1 = 0.88^{+0.09}_{-0.08}$, light ratio $L_2/L_1 = 0.64^{+0.10}_{-0.14}$, resulting stellar radii of $R_1 = 0.251^{+0.012}_{-0.008} R_\odot$, and $R_2 = 0.23^{+0.01}_{-0.02} R_\odot$. The results remain consistent with 1σ , with the radius uncertainties increased by a factor of ~ 1.5 .

3.2 Spectral classification

3.2.1 Effective temperature

We use the WiFeS low-resolution spectrum, which has the largest spectral coverage and highest S/N, to constrain the effective temperature of HATS551–027. Whilst the spectrum of HATS551–027 is a composite, at low resolution we cannot resolve the two binary components by their velocity differences. We first treat the spectral classification as if HATS551–027 is a single star.

The flux-calibrated WiFeS $R = 3000$ observation is matched to synthetic spectra from BT-Settl models (Allard et al. 2012) with Asplund et al. (2009) abundances. We fix $\log g$ to 5.0 (derived from Section 3.1.2 to be 4.99 and 5.01 for stars A and B, and consistent with stellar isochrone models, e.g. Dotter et al. 2008) and $[M/H]$ to 0.0, and minimize the χ^2 fit by varying T_{eff} at steps of 100 K, interpolating the $T_{\text{eff}}-\chi^2$ relationship with a B-spline.

First, to understand the uncertainties in our temperature classification, we obtained WiFeS spectra of five M-dwarfs with temperatures measured from interferometry observations. The WiFeS BT-Settl model fit temperatures and the interferometry temperatures are shown on Table 7. We find an error of 85 K encompasses 68 per cent of the deviations between the WiFeS measurements and literature values, weighted by the literature uncertainties. We find an error of 150 K when we use models employing the Caffau et al. (2011) abundances. We also tested the standard stars against models

Table 7. WiFeS M-dwarf spectral classifications.

Object	Literature T_{eff} (K)	WiFeS T_{eff} (K) ^a	Ref
GJ 191	3570 ± 156	3787	1
GJ 551	3098 ± 56	3000	2
GJ 699	3224 ± 10	3305	3
GJ 880	3713 ± 11	3671	3
GJ 887	3797 ± 45	3724	2

References: 1 – Ségransan et al. (2003); 2 – Demory et al. (2009); 3 – Boyajian et al. (2012).

Note. ^aMatched against BT-Settl spectral models using Asplund et al. (2009) abundances, with $[M/H] = 0.0$.

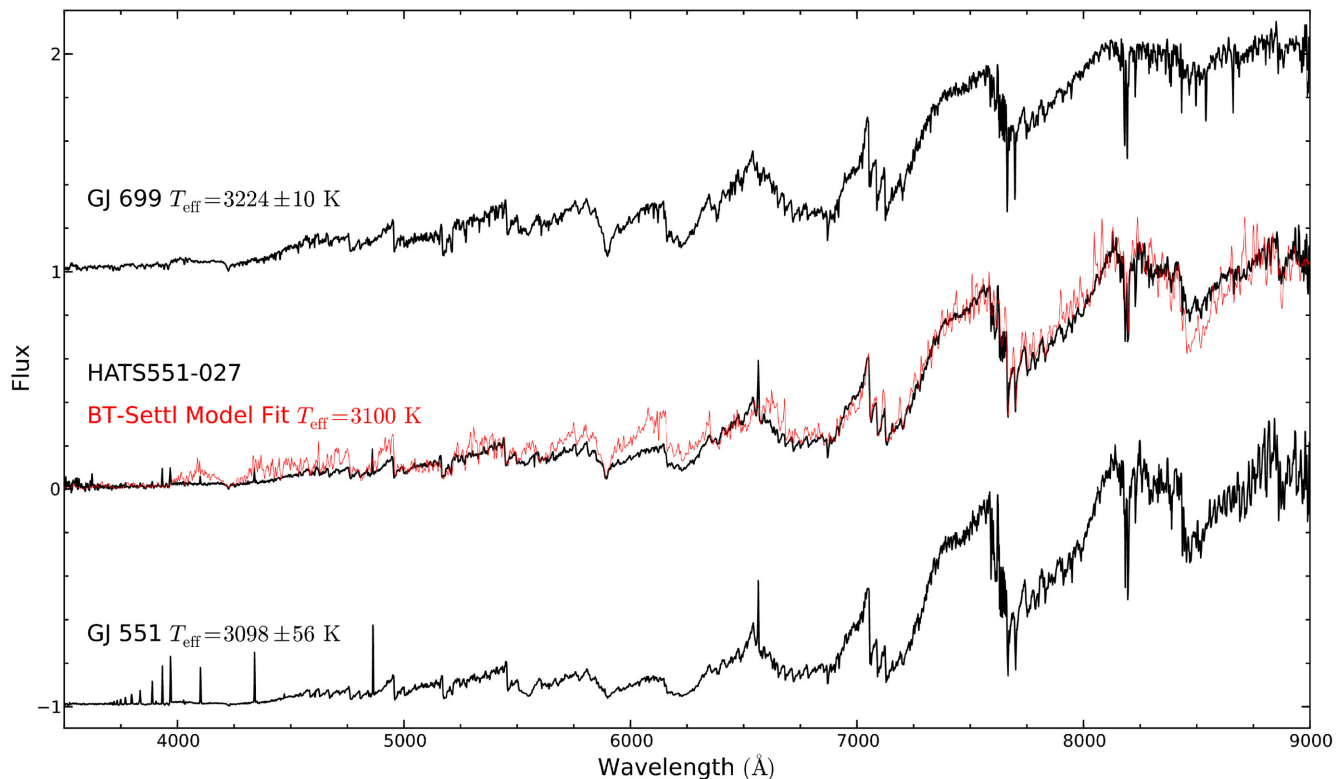


Figure 7. WiFeS $R = 3000$ spectra of HATS551–027 and two standard M-dwarfs of similar a spectral type, GJ 551 and GJ 699. The observations are plotted in black, best-fitting BT-Settl spectral model to HATS551–027 in red.

with metallicities of $[M/H] = -0.5, +0.3, \text{ and } +0.5$ (using Asplund et al. 2009 abundances). We found a mean error of 100, 85, and 95 K for each of the metallicities, respectively. The temperatures derived using the different metallicities differed systematically from that of the temperatures derived from the $[M/H] = 0.0$ models by $-40, +20, \text{ and } +60$ K, respectively.

For HATS551–027, we find a best-fitting binary effective temperature of $T_{\text{eff}} = 3113$ K. We discuss metallicity later in the section. The WiFeS spectrum and the best-fitting model are plotted in Fig. 7.

For comparison, we also plot in Fig. 7 the WiFeS spectra of GJ 551 (M5.5V 3098 ± 56 K; Demory et al. 2009) and GJ 699 (M4V 3224 ± 10 K; Boyajian et al. 2012), two M-dwarfs with similar temperatures and spectra as HATS551–027. A visual inspection of some temperature sensitive features, such as the depth of the TiO absorption bands, the Na and CaOH lines, confirms that HATS551–027 has a spectral type between the GJ 551 and GJ 699.

To estimate the temperatures of the two stellar components, we simultaneously fitted for the temperatures of both stellar components using a grid of simulated composite spectra. We generated a 2D grid of composite spectra from the BT-Settl models at steps of 100 K for both simulated stellar components, with fluxes scaled using the best-fitting radius ratio, and wavelength shifted in velocity according to the Keplerian orbit solution (both derived in Section 3.1). We then calculate the χ^2 of fit to the WiFeS spectrum and WiFeS CCF-derived light ratios in the R7000 and I7000 spectral bands (Section 2.3.1). The best-fitting component temperatures were $T_{\text{eff},1} = T_{\text{eff},2} = 3100$, consistent with the binary effective temperature.

We can also approximate the temperature of the two stellar components by assuming they follow the Stefan–Boltzmann law. We adopt a binary effective temperature of 3114 ± 85 K, light ratio of $0.50^{+0.10}_{-0.04}$, and the stellar radii from Table 6. The derived temperature ratio is 0.94 ± 0.04 , with the temperature of the primary stellar component as $T_{\text{eff},1} = 3190 \pm 100$ K and the secondary component as $T_{\text{eff},2} = 2990 \pm 110$ K. We adopt these temperature ratio derived temperatures for the further analysis.

3.2.2 Metallicity

Accurate metallicities for M-dwarfs are difficult to measure from optical spectra, since the molecular absorption features distort the continuum significantly, and mask out the common metal lines. We first use the ζ TiO/CaH index to estimate the metallicity of HATS551–027. We measure the band indices for TiO5, CaH2, and CaH3, according to the regions defined in Reid, Hawley & Gizis (1995), to be 0.36, 0.39, and 0.68, respectively. We calculate a series of ζ values using relations between CaH2+CaH3 and the $[\text{TiO}5]_{Z_{\odot}}$ index from calibrations in Lépine, Rich & Shara (2007), Dhital et al. (2012), and Lépine et al. (2013), all yielding $\zeta = 1.0$, the average abundance for disc stars. The derived metallicity estimate for HATS551–027 is $[M/H] = 0.0 \pm 0.2$ using the calibrations and uncertainties between ζ and $[M/H]$ from Mann et al. (2013). For a consistency check, we also use the metallicity, $J - K$ and $V - K$ colour relationships from Mann et al. (2013) to calculate a photometric colour-derived metallicity of $[M/H] = +0.1 \pm 0.2$, consistent with the band indices result. However, we note that infrared spec-

Table 8. HATS551–027 stellar parameters.

Parameter	Value	Source
RA (J2000 HH:MM:SS.SS)	05:44:57.92	2MASS
Dec. (J2000 DD:MM:SS.SS)	−24:56:09.6	2MASS
Proper motion (mas yr ^{−1} RA Dec.)	229 −25	Salim & Gould (2003)
Proper motion error ellipse (mas yr ^{−1} mas yr ^{−1} Position angle)	5 5 104	Salim & Gould (2003)
Photometric parameters		
<i>B</i> (mag)	17.3 ± 0.1	APASS
<i>g</i> ' (mag)	16.3	APASS
<i>V</i> (mag)	15.54 ± 0.05	APASS
<i>r</i> ' (mag)	15.0	APASS
<i>i</i> ' (mag)	13.221 ± 0.05	APASS
<i>J</i> (mag)	10.75 ± 0.02	2MASS
<i>H</i> (mag)	10.13 ± 0.02	2MASS
<i>K</i> (mag)	9.85 ± 0.02	2MASS
Spectroscopic parameters		
<i>T</i> _{eff, 1} (K)	3190 ± 100	WiFeS
<i>T</i> _{eff, 2} (K)	2990 ± 110	WiFeS
[<i>M</i> / <i>H</i>]	0.0 ± 0.2	WiFeS
log <i>L</i> _{Hα, 1} / <i>L</i> _{bol, 1}	−4.15 ± 0.03	PFS
log <i>L</i> _{Hα, 2} / <i>L</i> _{bol, 2}	−4.08 ± 0.05	PFS

troscopy will be necessary to provide a definitive measurement for the metallicity of HATS551–027.

3.2.3 Activity and *H*α emission

The low-resolution WiFeS spectrum of HATS551–027 shows all the Balmer lines, and the calcium H&K lines, in emission. The strength of *H*α emission is commonly interpreted as an indicator for stellar activity, and potentially correlated to the inflated radii of M-dwarfs (López-Morales 2007; Stassun et al. 2012). We use the PFS spectra to measure the equivalent width of the *H*α emission for both stellar components of the binary, fitting Gaussian profiles to each feature. We calculate the equivalent width by assuming a polynomial fit to the continuum flux, scaled to the relative light contribution from each stellar component ($L_2/L_1 = 0.56^{+0.06}_{-0.06}$; Section 3.1). The measured equivalent widths are $2.8 \pm 0.2 \text{ \AA}$ and $3.6 \pm 0.4 \text{ \AA}$ for HATS551–027A and B, respectively. To calculate the $L_{H\alpha}/L_{Bol}$ ratio for each stellar component, we measure an L_{Bol} for each stellar component by integrating under the respective best-fitting BT-Settl model spectra. The $L_{H\alpha}/L_{Bol}$ ratio is calculated by comparing the flux of the Gaussian fit to the *H*α lines to the integrated fluxes of the BT-Settl models. The largest error contribution comes from the L_{Bol} estimate, stemming from the uncertainty in the atmospheric parameters. To estimate the uncertainty, we calculate a series of $L_{H\alpha}/L_{Bol}$ values for each component whilst adopting a grid of spectral models, with $T_{eff, 1}$ from 3000 to 3200 K, and $T_{eff, 2}$ from 2900 to 3100 K. The standard deviation scatter in the resulting $L_{H\alpha}/L_{Bol}$ is adopted as the uncertainty. The derived $L_{H\alpha}/L_{Bol}$ are -4.15 ± 0.03 and -4.08 ± 0.05 for the two stellar components.

The set of stellar photometric and spectroscopic parameters for HATS551–027 are presented in Table 8.

4 DISCUSSION

Following CM Draconis and KOI-126, HATS551–027 is the third well-characterized double-lined eclipsing binary with both components in the fully convective regime. Fig. 8 shows the masses, radii,

and temperatures of the HATS551–027 system with respect to other well-characterized double-lined eclipsing binaries in the same mass regime. Fig. 8 also compares the properties of HATS551–027 to isochrones from the Dartmouth (Dotter et al. 2008), Baraffe et al. (1998), PARSEC models (Bressan et al. 2012; Chen et al. 2014), and Yonsei–Yale (YY, Yi et al. 2001; Spada et al. 2013) models.

The radius and estimated temperatures of these binaries are largely discrepant to the Dartmouth, YY, and Baraffe et al. (1998) models, but generally agree with the PARSEC model predictions to $\sim 1\sigma$. Compared to the Dartmouth 5 Gyr isochrones, the observed radii for the HATS551–027 system are larger by 2.6 ± 3.5 and 9.1 ± 4.8 per cent for components A and B, respectively; the temperatures are cooler by 3.8 ± 3.6 and 7.9 ± 3.7 per cent, respectively. The measured system properties are more consistent to the PASCAR 5 Gyr isochrones, the observed radius of component A is smaller than the models by 0.6 ± 3.6 per cent, and component B larger than the model by 4.2 ± 4.9 per cent, both consistent within errors. The temperatures for both components are also consistent to within errors, with A and B hotter than the models by 3.1 ± 5.0 and 2.6 ± 5.6 per cent, respectively. The uncertainties are derived via a Monte Carlo exercise, drawing the observed sample from Gaussian distributions based on the measurement errors in mass, radius, and metallicity. For trials with subsolar metallicities, we interpolate between the $[M/H] = -0.5$ and 0.0 isochrones to derive the model radius; for supersolar metallicities, we interpolate between the $[M/H] = 0.0$ and +0.5 isochrones.

For tidally locked binaries, a shorter orbital period, and thereby rotation period, may lead to more powerful internal dynamos. In turn, the higher stellar activity may result in a greater discrepancy between the observed properties of these binaries and their model predictions. Fleming, Gioia & Maccacaro (1989) established a rotation – X-ray activity correlation for main sequence single stars. López-Morales (2007) and Stassun et al. (2012) demonstrated a correlation between X-ray activity and the radius, T_{eff} discrepancy of low-mass binaries.

HATS551–027 has a significantly longer period (4.1 d) than both CM Draconis and KOI-126 BC (< 2 d). However, there appears to be no direct correlation between the model discrepancy and

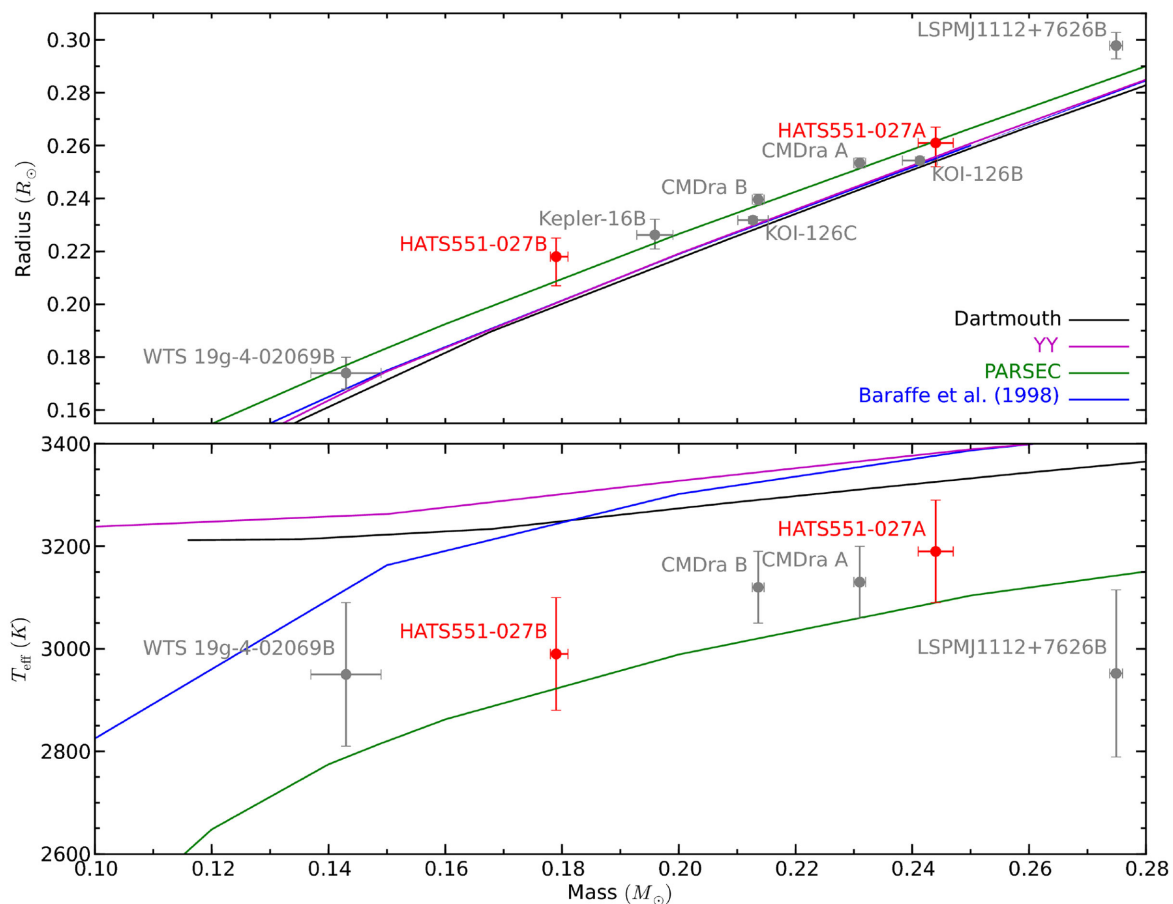


Figure 8. The measured masses, radii, and temperatures of the well-characterized double-line eclipsing binaries with respect to the model isochrones. Solar metallicity, 5 Gyr models from Dartmouth (Dotter et al. 2008) are plotted in black, Yonsei–Yale (Yi et al. 2001; Spada et al. 2013) in magenta, PARSEC (Bressan et al. 2012; Chen et al. 2014) in green, and Baraffe et al. (1998) in blue. Stellar properties for CM Draconis are taken from Morales et al. (2009), KOI-126 BC from Carter et al. (2011), the radii of Kepler-16 B from Doyle et al. (2011) and dynamical masses from Bender et al. (2012), LSPM1112+7626 B from Irwin et al. (2011), and WTS 19g-4-02069 B from Nefs et al. (2013).

orbital period. In the HATS551–027 system, only HATS551–027B is significantly inflated. In the short period (1.3 d) CM Draconis binary, both stellar components are discrepant from the models in radius and temperature (Torres & Ribas 2002; MacDonald & Mullan 2012; Spada et al. 2013; Feiden & Chaboyer 2014). Compared to the Dartmouth 5 Gyr isochrones, the radii of the CM Draconis stars (adopting parameters from Morales et al. 2009) are inflated by 5.5 ± 1.0 and 6.1 ± 1.1 per cent, and temperatures cooler by 8.0 ± 2.3 and 7.6 ± 2.3 per cent for components A and B, respectively. However, standard isochrone models can reproduce the radii of the KOI-126 BC system very well (e.g. Feiden et al. 2011; Spada & Demarque 2012), even though it is a similar close-in binary system with period of 1.8 d. Compared to the Dartmouth models, KOI-126 B is negligibly smaller by 0.2 ± 1.2 per cent, and C is negligibly larger by 0.5 ± 1.3 per cent.

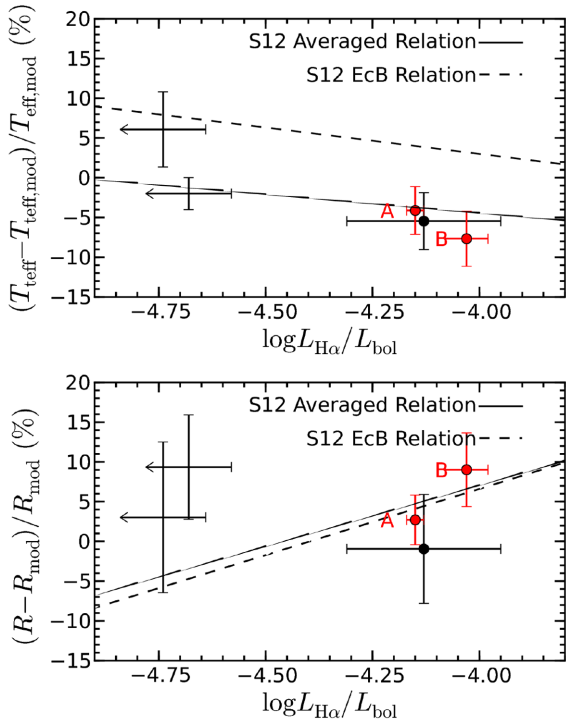
A lack of correlation remains when we also consider well-characterized double-line eclipsing binaries with one low-mass component. LSPMJ1112+7626 (Irwin et al. 2011) has a long period of ~ 41 d, with both components of the binary significantly inflated in radius by ~ 5 per cent, and cooler in temperature by ~ 10 per cent compared to standard models. Kepler-16, another 41 d period unequal mass binary (Doyle et al. 2011) is also inflated in comparison

to models by ~ 7 per cent if we adopt the dynamical masses measured by Bender et al. (2012). This is consistent with the findings of Feiden & Chaboyer (2012), which showed a lack of period correlation for detached double-lined eclipsing binaries. Zhou et al. (2014) also examined a larger sample of double-lined and single-lined binaries in $< 0.3 M_{\odot}$ regime, finding no correlations with period.

We also examine $H\alpha$, as a direct activity indicator, for correlations against the radius and T_{eff} -model discrepancies. The stellar components of HATS551–027 show $H\alpha$ emissions and spot modulation, signatures of significant stellar activity. Both components of HATS551–027 exhibit discrepancies in the T_{eff} with respect to the Dartmouth models. CM Draconis system is also known to be active from its spot modulations (Morales et al. 2009) and X-ray emission (López-Morales 2007). Although we lack a directly measured $H\alpha$ emission of CM Draconis, we can estimate the $H\alpha$ flux by converting the X-ray fluxes of CM Draconis reported by López-Morales (2007) to $\log L_{H\alpha}/L_{\text{bol}}$ using the empirical relationship established for field M-dwarfs in Stassun et al. (2012). The approximate $H\alpha$ fluxes are $\log L_{H\alpha}/L_{\text{bol}} = -3.8^{+1.2}_{-1.8}$ for CM Draconis A, and $-3.7^{+1.2}_{-1.8}$ for B, similar to the $H\alpha$ activity we measure for HATS551–027. WTS 19g-4-02069 (Nefs et al. 2013) was also reported to exhibit strong $H\alpha$ emission and T_{eff} -model

Table 9. $H\alpha$ emission strength measured from WiFeS spectra.

Object	$\log L_{H\alpha}/L_{bol}$
GJ191	<-4.69
GJ551	-4.13 ± 0.18
GJ699	<-4.63
HATS551–027A	-4.15 ± 0.02
HATS551–027B	-4.03 ± 0.05

**Figure 9.** The $H\alpha$ emission strength ($\log L_{H\alpha}/L_{bol}$) for the five VLMSs (Table 9) are plotted with respect to their radius and temperature deviation from the 5-Gyr solar metallicity Dartmouth isochrone. The measurements for HATS551–027 are plotted in red, with the two stellar components labelled. We also plot the empirical relationships derived by Stassun et al. (2012, S12 in the plot labels) using M-dwarfs ($< 0.6 M_{\odot}$) with $H\alpha$ emission strength derived from X-ray fluxes for comparison.

discrepancy, but we could not estimate $\log L_{H\alpha}/L_{bol}$ value from the reports. One exception to this trend is LSPM J1112+7626B, which has no reported $H\alpha$ emission (Irwin et al. 2011), but an estimated temperature discrepant with the Dartmouth at ~ 6 per cent.

We also measure the $\log L_{H\alpha}/L_{bol}$ for the single stars GJ 191, GJ 551, and GJ 699 from the WiFeS spectra that we took for spectral classifications (Section 3.2.1). GJ 551 exhibits a distinct $H\alpha$ emission feature, but we can only provide 1σ upper limits for the $H\alpha$ strength of GJ 191 and GJ 699 (Table 9).

Fig. 9 plots the $\log L_{H\alpha}/L_{bol}$ values of HATS551–027 and the single stars against the temperature and radius discrepancy of the respective stars. For reference, we also plot the empirical correlations found by Stassun et al. (2012). Whilst the small sample size (3) prevents any meaningful statistical interpretation, we note that the $T_{eff}-\log L_{H\alpha}/L_{bol}$ relationship appears to be consistent to this analysis for the VLMSs. The two stars without apparent $H\alpha$ emission, GJ 191 and GJ 699, have effective temperatures hotter than the three stars with $H\alpha$ emission features, GJ 551,

HATS551–027A and B. This is potentially indicative that the M-dwarfs with cooler photospheric temperatures have hotter chromospheric temperatures.

Given the smaller model-observation discrepancy in radius, we cannot confirm a radius– $H\alpha$ activity relationship from this sample. More double-lined binaries with $H\alpha$ or X-ray measurements need to be made to confirm these relationships. In addition, $H\alpha$ activity cannot be the sole cause of the radius excess, given that HATS551–027A and B exhibit similar $H\alpha$ activity, but only B exhibits a radius excess to the isochrones. Irwin et al. (2011) also note a lack of detectable $H\alpha$ emission features for LSPM J1112+7626, despite the inflated radii for both components of the binary.

The HATS551–027 system is also unique as the only very low mass M–M binary well positioned for Southern hemisphere facilities. This should enable a host of follow-up opportunities to better characterize the properties of this benchmark system.

ACKNOWLEDGEMENTS

Development of the HATSouth project was funded by NSF MRI grant NSF/AST-0723074, operations are supported by NASA grant NNX12AH91H, and follow-up observations receive partial support from grant NSF/AST-1108686. Work at the Australian National University is supported by ARC Laureate Fellowship Grant FL0992131. Follow-up observations with the MPG 2.2 m/FEROS instrument were performed under MPIA guaranteed time (P087.A-9014(A), P088.A-9008(A), P089.A-9008(A)) and Chilean time (P087.C-0508(A)). AJ acknowledges support from project IC120009 ‘Millennium Institute of Astrophysics (MAS)’ of the Millennium Science Initiative, Chilean Ministry of Economy, FONDECYT project 1130857, and BASAL CATA PFB-06. VS acknowledges support from BASAL CATA PFB-06. RB and NE acknowledge support from CONICYT-PCHA/Doctorado Nacional and Fondecyt project 1130857. KP acknowledges support from NASA grant: NNX13AQ62G. This work is based on observations made with ESO Telescopes at the La Silla Observatory under programme IDs P087.A-9014(A), P088.A-9008(A), P089.A-9008(A), P087.C-0508(A), and 089.A-9006(A). We acknowledge the use of the AAVSO Photometric All-Sky Survey (APASS), funded by the Robert Martin Ayers Sciences Fund, and the SIMBAD data base, operated at CDS, Strasbourg, France. Operations at the MPG/ESO 2.2 m Telescope are jointly performed by the Max Planck Gesellschaft and the European Southern Observatory. The imaging system GROND has been built by the high-energy group of MPE in collaboration with the LSW Tautenburg and ESO. We thank Régis Lachaume for his technical assistance during the observations at the MPG 2.2 m Telescope. Australian access to the Magellan Telescopes was supported through the National Collaborative Research Infrastructure Strategy of the Australian Federal Government. We thank Albert Jahnke, Toni Hanke (HESS), Peter Conroy (MSO) for their contributions to the HATSouth project.

The HATSouth network is operated by a collaboration consisting of Princeton University (PU), the Max Planck Institut für Astronomie (MPIA), the Australian National University (ANU), and the Pontificia Universidad Católica de Chile (PUC). The station at Las Campanas Observatory (LCO) of the Carnegie Institution is operated by PU in conjunction with PUC, the station at the High Energy Spectroscopic Survey (HESS) site is operated in conjunction with MPIA, and the station at Siding Spring Observatory (SSO) is operated jointly with ANU. This paper includes data gathered with the 6.5 metre Magellan Telescopes located at Las Campanas Observatory, Chile.

REFERENCES

- Allard F., Homeier D., Freytag B., Sharp C. M., 2012, *EAS Publ. Ser.*, 57, 3
- Asplund M., Grevesse N., Sauval A. J., Scott P., 2009, *ARA&A*, 47, 481
- Bakos G. Á. et al., 2007, *ApJ*, 670, 826
- Bakos G. Á. et al., 2013, *PASP*, 125, 154
- Chabrier I., Chabrier G., Allard F., Hauschildt P. H., 1998, *A&A*, 337, 403
- Bayliss D. et al., 2013, *AJ*, 146, 113
- Bender C. F. et al., 2012, *ApJ*, 751, L31
- Berger D. H. et al., 2006, *ApJ*, 644, 475
- Bertin E., Arnouts S., 1996, *A&AS*, 117, 393
- Bessell M. S., 1999, *PASP*, 111, 1426
- Boyajian T. S. et al., 2012, *ApJ*, 757, 112
- Brahm R. et al., 2015, preprint ([arXiv:1503.00062](https://arxiv.org/abs/1503.00062))
- Bressan A., Marigo P., Girardi L., Salasnich B., Dal Cero C., Rubele S., Nanni A., 2012, *MNRAS*, 427, 127
- Burrows A., Heng K., Nampaisarn T., 2011, *ApJ*, 736, 47
- Caffau E., Ludwig H.-G., Steffen M., Freytag B., Bonifacio P., 2011, *Sol. Phys.*, 268, 255
- Carter J. A. et al., 2011, *Science*, 331, 562
- Chabrier G., Baraffe I., 1995, *ApJ*, 451, L29
- Chabrier G., Baraffe I., 1997, *A&A*, 327, 1039
- Chabrier G., Baraffe I., 2000, *ARA&A*, 38, 337
- Chabrier G., Gallardo J., Baraffe I., 2007, *A&A*, 472, L17
- Chen Y., Girardi L., Bressan A., Marigo P., Barbieri M., Kong X., 2014, *MNRAS*, 444, 2525
- Claret A., 2000, *A&A*, 363, 1081
- Crane J. D., Shectman S. A., Butler R. P., Thompson I. B., Birk C., Jones P., Burley G. S., 2010, in McLean I. S., Ramsay S. K., Takami H., eds, *Proc. SPIE Conf. Ser. Vol. 7735, Ground-based and Airborne Instrumentation for Astronomy III*. SPIE, Bellingham, p. 773553
- Demory B.-O. et al., 2009, *A&A*, 505, 205
- Dhital S., West A. A., Stassun K. G., Bochanski J. J., Massey A. P., Bastien F. A., 2012, *AJ*, 143, 67
- Dopita M., Hart J., McGregor P., Oates P., Bloxham G., Jones D., 2007, *Ap&SS*, 310, 255
- Dotter A., Chaboyer B., Jevremović D., Kostov V., Baron E., Ferguson J. W., 2008, *ApJS*, 178, 89
- Doyle L. R. et al., 2011, *Science*, 333, 1602
- Feiden G. A., Chaboyer B., 2012, *ApJ*, 757, 42
- Feiden G. A., Chaboyer B., 2014, *ApJ*, 789, 53
- Feiden G. A., Chaboyer B., Dotter A., 2011, *ApJ*, 740, L25
- Fleming T. A., Gioia I. M., Maccacaro T., 1989, *ApJ*, 340, 1011
- Foreman-Mackey D., Hogg D. W., Lang D., Goodman J., 2013, *PASP*, 125, 306
- Gibson N. P., Aigrain S., Roberts S., Evans T. M., Osborne M., Pont F., 2012, *MNRAS*, 419, 2683
- Hamuy M., Walker A. R., Suntzeff N. B., Gigoux P., Heathcote S. R., Phillips M. M., 1992, *PASP*, 104, 533
- Hartman J. D. et al., 2015, *AJ*, 149, 166
- Huang X., Bakos G. Á., Hartman J. D., 2013, *MNRAS*, 429, 2001
- Irwin J. M. et al., 2011, *ApJ*, 742, 123
- Johnson J. A. et al., 2011, *ApJ*, 730, 79
- Johnson J. A. et al., 2012, *AJ*, 143, 111
- Jordán A. et al., 2014, *AJ*, 148, 29
- Kovács G., Zucker S., Mazeh T., 2002, *A&A*, 391, 369
- Kovács G., Bakos G., Noyes R. W., 2005, *MNRAS*, 356, 557
- Lacy C. H., 1977, *ApJ*, 218, 444
- Lépine S., Rich R. M., Shara M. M., 2007, *ApJ*, 669, 1235
- Lépine S., Hilton E. J., Mann A. W., Wilde M., Rojas-Ayala B., Cruz K. L., Gaidos E., 2013, *AJ*, 145, 102
- Lomb N. R., 1976, *Ap&SS*, 39, 447
- López-Morales M., 2007, *ApJ*, 660, 732
- Luyten W. J., 1979, *New Luyten Catalogue of Stars with Proper Motions Larger Than Two Tenths of an Arcsecond*. Univ. Minneapolis, Minnesota
- MacDonald J., Mullan D. J., 2012, *MNRAS*, 421, 3084
- MacDonald J., Mullan D. J., 2014, *ApJ*, 787, 70
- Mann A. W., Brewer J. M., Gaidos E., Lépine S., Hilton E. J., 2013, *AJ*, 145, 52
- Metcalfe T. S., Mathieu R. D., Latham D. W., Torres G., 1996, *ApJ*, 456, 356
- Morales J. C., Ribas I., Jordi C., 2008, *A&A*, 478, 507
- Morales J. C. et al., 2009, *ApJ*, 691, 1400
- Nefs S. V. et al., 2013, *MNRAS*, 431, 3240
- Nelson B., Davis W. D., 1972, *ApJ*, 174, 617
- Pál A., 2012, *MNRAS*, 421, 1825
- Penev K. et al., 2013, *AJ*, 145, 5
- Popper D. M., Etzel P. B., 1981, *AJ*, 86, 102
- Reid I. N., Hawley S. L., Gizis J. E., 1995, *AJ*, 110, 1838
- Reid I. N. et al., 2003, *AJ*, 126, 3007
- Ribas I., 2006, *Ap&SS*, 304, 89
- Salim S., Gould A., 2003, *ApJ*, 582, 1011
- Scargle J. D., 1982, *ApJ*, 263, 835
- Ségransan D., Kervella P., Forveille T., Queloz D., 2003, *A&A*, 397, L5
- Southworth J., Maxted P. F. L., Smalley B., 2004, *MNRAS*, 351, 1277
- Spada F., Demarque P., 2012, *MNRAS*, 422, 2255
- Spada F., Demarque P., Kim Y.-C., Sills A., 2013, *ApJ*, 776, 87
- Stassun K. G., Kratter K. M., Scholz A., Dupuy T. J., 2012, *ApJ*, 756, 47
- Torres G., 2013, *Astron. Nachr.*, 334, 4
- Torres G., Ribas I., 2002, *ApJ*, 567, 1140
- Torres G., Andersen J., Giménez A., 2010, *A&AR*, 18, 67
- Yi S., Demarque P., Kim Y.-C., Lee Y.-W., Ree C. H., Lejeune T., Barnes S., 2001, *ApJS*, 136, 417
- Zhou G. et al., 2014, *MNRAS*, 437, 2831

SUPPORTING INFORMATION

Additional Supporting Information may be found in the online version of this article:

Table 2. HATS551–027 differential photometry. (<http://www.mnras.oxfordjournals.org/lookup/suppl/doi:10.1093/mnras/stv1070/-/DC1>).

Please note: Oxford University Press is not responsible for the content or functionality of any supporting materials supplied by the authors. Any queries (other than missing material) should be directed to the corresponding author for the paper.

This paper has been typeset from a $\text{\TeX}/\text{\LaTeX}$ file prepared by the author.